Broadband Polarization-Conversion Metasurface for a Cassegrain Antenna with High Polarization Purity

Wen-Long Guo,[1,2] Guang-Ming Wang,[1] Ke Chen,[2] Hai-Peng Li,[1] Ya-Qiang Zhuang,[3] He-Xiu Xu,[1,*] and Yijun Feng[2,†]

[1] *Air and Missile Defense College, Air Force Engineering University, Xi'an 710051, China*

[2] *Department of Electronic Engineering, School of Electronic Science and Engineering, Nanjing University, Nanjing 210093, China*

[3] *Science and Technology on Complex Aviation Systems Simulation Laboratory, Beijing 100076, China*

(Received 26 February 2019; revised manuscript received 13 May 2019; published 3 July 2019)

Polarization conversion has been widely explored in the study of metasurfaces in order to achieve broad operation bandwidths, but its application is still restricted to a few practical scenarios. We design a broadband cross-polarization conversion metasurface and apply it to form a directionally radiated Cassegrain antenna with a low profile and high polarization purity. A quasi-l-shaped meta-atom is first optimized with both high cross-polarization conversion efficiency and a full span of phase modulation in a broad bandwidth. With a hyperbolic phase profile imposed on the surface, a metasurface is engineered that can conduct both focusing and polarization conversion into its cross-polarization component. Then, by introducing a polarized grating as a subreflector and simultaneously fixing the designed metasurface as the main reflector, a planar Cassegrain antenna is facilitated with a low profile, high gain, and high polarization purity in a broad frequency band. This strategy of broad-band polarization conversion and its attempt to design a Cassegrain antenna lays a foundation for high-performance functional devices, promising great potential in real-world applications.

DOI: 10.1103/PhysRevApplied.12.014009

I. INTRODUCTION

The manipulation of the polarization state of electromagnetic (EM) waves at will is a research hotspot since many fascinating phenomena are inherently sensitive to polarization [1–3]. Conventional devices engineered for such a purpose are mostly based on birefringent crystals of Faraday effects [4], which are typically bulky in size. Fortunately, the recently developed planar two-dimensional metasurfaces (MSs), which are composed of artificially designed subwavelength meta-atoms [5–8], afford an effective strategy to manipulate the polarization state of em waves with low cost, low loss, and low profile [9,10]. Moreover, metasurfaces have also been proven to be an efficient method to realize many exotic phenomena and functionalities, such as negative reflection and/or refraction [11], superlens [12,13], vortex beam generator [14–16], invisible cloak [17–19], and so on.

For the MS-based linear cross-polarization conversion (cross-PC), two main approaches are available for high efficiency [20–24]. The first is to use anisotropic MSs to divide an incoming wave into two orthogonally polarized counterparts and then generate a proper phase difference between them [20–22]. The other is to utilize chiral MSs to mimic molecule chirality [23,24]. Following the above two methods, substantial efforts have been devoted to enhancing the working bandwidth. For example, different meta-atoms, such as double V shaped patches [25], cut-wire structures [26], and ring and/or disk cavities [9], have been proposed to expand the operation bandwidth. In addition to the band-width issue, efforts have also been concentrated on engineering applications, especially for antennas [27–30]. This is especially true for circularly polarized (CP) radiation [27] and polarization-reconfigurable antennas [28]. In addition, the cross-PC MSs consisting of meta-atoms of 0° and 90° rotation that exhibit a 1-bit phase change are also applied to suppress the backward radar cross section of a patch antenna [29]. Most recently, cross-polarization converters with simultaneous amplitude and phase control have also been realized for applications such as main- and side-lobe control [30], Airy beam, and dual focusing [31]. Nevertheless, the application of PC MSs to the engineering of wide-band Cassegrain [32,33] radiation while simultaneously embracing a low profile, high gain, and high polarization purity is rarely reported.

Here, we report a concept to devise a broad-band polarization converter for a Cassegrain antenna with a

*hxxuellen@gmail.com
†yjfeng@nju.edu.cn

low profile and high polarization purity. A quasi-l-shaped meta-atom operating in the reflection mode is first optimized with a broad-band cross-PC and a simultaneous near-360° phase cover, and then it is engineered to configure a focusing MS lens. By introducing a polarized grating as the subreflector and setting the designed MS as the main reflector, a Cassegrain antenna is finally assembled with a low profile, broad bandwidth, high gain, and high polarization purity. With these good performances, the proposed antenna will be promising for many applications, such as satellite communication, radar systems, the next generation of mobile communication system, and so on.

II. CONCEPT AND META-ATOM DESIGN

A. Concept of the cross-PC metasurface and its Cassegrain application

For a constituent meta-atom of a MS, two Jones matrices can be employed to describe its EM characteristics [34]. Specifically, the respective matrices for reflection and transmission are

$$\mathbf{R} = \begin{pmatrix} R_{xx} & R_{xy} \\ R_{yx} & R_{yy} \end{pmatrix}, \quad \mathbf{T} = \begin{pmatrix} T_{xx} & T_{xy} \\ T_{yx} & T_{yy} \end{pmatrix}. \tag{1}$$

Here, the analysis is conducted on the basis that all em waves can be decomposed into two orthogonally polarized waves, namely x and y polarized waves. The cross-PC MS operating in reflection geometry, which is shown in Fig. 1(a), always has Jones matrix $\mathbf{R} = \begin{pmatrix} 0 & \exp(j\Phi_0) \\ \exp(j\Phi_0) & 0 \end{pmatrix}$. With size modulation of the element, the cross-polarized phase shift of Φ_0 will be a variable and thus can be described as $\Phi(r, \theta, \varphi \ldots)$, where $r, \theta, \varphi \ldots$ are the size parameters of the element. Notably, the meta-atom can always hold high cross-polarization reflectivity when the sizes of $r, \theta, \varphi \ldots$ are modulated. In addition, the phase profile described as $\Phi(x, y) = (2\pi/\lambda)(\sqrt{x^2 + y^2 + F^2} - F)$ is the key point to design a planar focusing MS, where F indicates the focal length of the MS. Translating the phase profile into corresponding elements, we can configure a focusing MS with simultaneous PC effect, which is unambiguously shown in Fig. 1(b). In Fig. 1(c), we show the operating mechanism of a polarized grating (PG). It should be noted that the left hand circularly polarized (LHCP) wave in Fig. 1(c) is used to indicate the incident wave containing both x and y polarized components. Clearly, the PG is capable of reflecting y and transmitting x polarization with high efficiency. Finally, the working principle of the so-called planar Cassegrain antenna is clearly depicted in Fig. 1(d), where the subreflector of "PG" is the surface depicted in Fig. 1(c) and the main reflector of "PC FMS" is the PC focusing MS (PC FMS) shown in Fig. 1(b).

The operating process of the antenna can be described as follows. First, a y polarized spherical wave emitted from the feed source (FS) impinges on the PG and is then specularly reflected to the PC FMS. By setting a proper distance between the PG and PC FMS, a virtual FS is equivalently generated and exactly located at the focal point of the PC FMS according to the mirror image theory. Then, the y polarized wave reflected from the PG will illuminate the PC FMS and then be reflected into the x polarized plane wave due to the PC effect and the wave-front tailoring

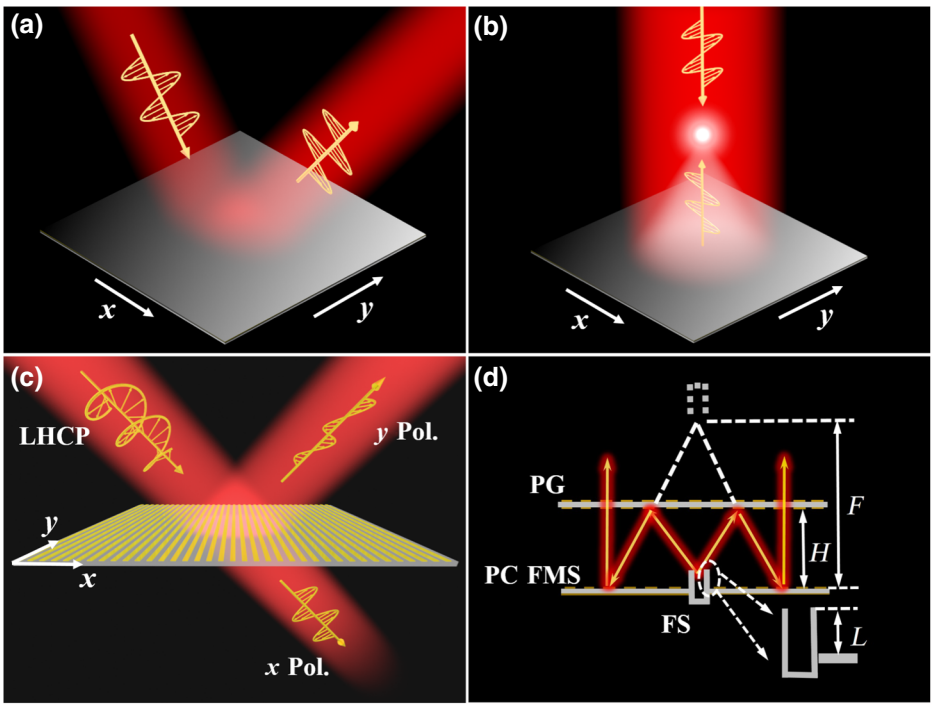

FIG. 1. Schematic view of the polarization converter and its application to Cassegrain antenna design. (a) The cross-polarization conversion MS to convert y polarized incidence into x polarized mode. (b) The cross-polarized conversion focusing MS (PC FMS). (c) The PG with the abilities of reflecting y and transmitting x polarization. (d) The operating mechanism and side view of the assembled Cassegrain antenna. Note that the dashed gray lines depicted in (d) indicate a virtual FS formed by the principle of mirror images.

by the PC FMS. Finally, the x polarized plane wave will penetrate the PG with little loss and ultimately form a high-gain pencil beam in the far-field region. Based on this, the configuration of the main and subreflector will be determined by the principle of a mirror image. As illustrated in Fig. 1(d), the profile height of the proposed Cassegrain antenna can be described as

$$H = \frac{F + L}{2}, \tag{2}$$

where F is the focal length of the PC FMS and L represents the outstretched distance of the waveguide FS.

B. Meta-atom design

Based on the abovementioned analysis, a broad-band PC meta-atom should first be configured. As shown in Figs. 2(a) and 2(b), a classical quasi-l-shaped meta-atom [35] is optimized to realize a broadband PC effect. In particular, the concrete sizes of the element are denoted by $p = 5$ mm, $h = 2.5$ mm, $d = 0.3$ mm, $d_1 = 0.4$ mm, $r = 1.6$ mm, $\theta = 45°$, and $\varphi = 120°$. The quasi-l-shaped metallic pattern is diagonally etched on a dielectric substrate with a relative permittivity of 2.65 and loss tangent of 0.003. In addition, the dielectric substrate is backed by a metallic layer with a thickness of 0.036 mm to ensure the meta-atom is operating in reflection geometry. To give a comprehensive understanding of the PC principle, we assume that the element is first arranged as in Fig. 2(c) and impinged by a y polarized plane wave.

On that basis, the incident wave can be described as $\vec{E}^{\text{inc}} = E_0\hat{y} = E_0(\hat{u} + \hat{v})/\sqrt{2}$. Since the element is mirror symmetric with respect to the u and v axes, the reflection coefficients for the cross-polarized mode in the u-o-v coordinate system, which are denoted by R_{uv} and R_{vu}, are all suppressed to zero.

Correspondingly, the copolarized reflection coefficients denoted by R_{uu} and R_{vv} are all enhanced to 100% for a lossless case, so they can consequently be written as

$$R_{uu} = \exp(j\Phi_u), \quad R_{vv} = \exp(j\Phi_v), \tag{3}$$

where Φ_u and Φ_v are the copolarized reflection phase response for the u and v polarized incident waves, respectively. The reflected wave then becomes $\vec{E}^{\text{ref}} = E_0[\hat{u}\exp(j\Phi_u) + \hat{v}\exp(j\Phi_v)]/\sqrt{2}$. Translating u and v unit vectors into x and y unit vectors, we obtain $\hat{u} = (\hat{x} + \hat{y})/\sqrt{2}$, $\hat{v} = (\hat{y} - \hat{x})/\sqrt{2}$. Thus, the reflected wave can be described with x and y vectors as

$$\vec{E}^{\text{ref}} = \frac{E_0}{2}\{\hat{x}[\exp(j\Phi_u) - \exp(j\Phi_v)] + \hat{y}[\exp(j\Phi_u) + \exp(j\Phi_v)]\}. \tag{4}$$

Based on this, the reflection coefficients in the x-o-y coordinate system can be derived as

$$R_{yy} = \frac{\exp(j\Phi_u) + \exp(j\Phi_v)}{2}, \quad R_{xy} = \frac{\exp(j\Phi_u) - \exp(j\Phi_v)}{2}. \tag{5}$$

In addition, the PC ratio, denoted by R_{PC}, is commonly utilized to describe the conversion efficiency of the PC and can be defined

$$R_{\text{PC}} = \frac{R_{xy}^2}{R_{xy}^2 + R_{yy}^2}. \tag{6}$$

Since the element has a metallic layer at the bottom, if we suppose it is lossless, $R_{xy}^2 + R_{yy}^2$ will become unity according to the law of energy conservation. Then, the R_{PC} can

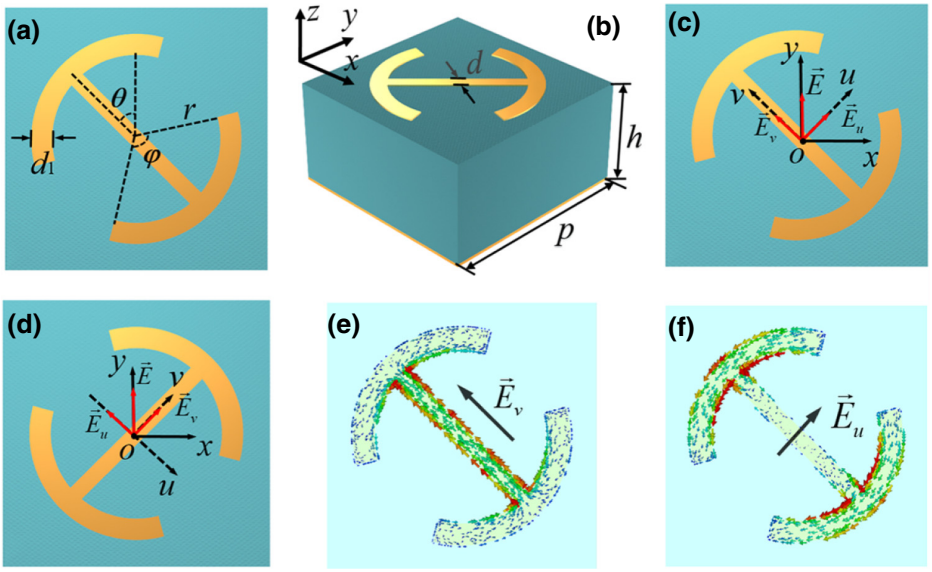

FIG. 2. The proposed meta-atom and its symmetric and asymmetric operation mode. (a) Top view and (b) perspective view. (c),(d) depict the E field analysis for the element with rotation angles of $\theta = 45°$ and $\theta = -45°$, respectively. (e),(f) are the surface current distributions under v and u polarized wave illumination, respectively. Element simulations are all carried out with unit-cell boundary in CST Microwave Studio.

be determined by $R_{PC} = R_{xy}^2 = 1 - R_{yy}^2$. We set $R_{PC} \geq 0.9$ as the criterion for the high-PC effect. Employing R_{yy} to express this criterion, we get

$$|R_{yy}| \leq -10 \text{ dB}. \tag{7}$$

Substituting Eq. (5) into Eq. (7) and assuming $\Delta\Phi = \Phi_u - \Phi_v$, we get $180° - 37° \leq |\Delta\Phi| \leq 180° + 37°$. To validate this criterion, we simulate and depict the copolarized reflectivity of $|R_{yy}|$ and the phase difference of $\Delta\Phi$ in Fig. 3. Clearly, the bandwidth of $|R_{yy}| \leq -10$ dB exactly coincides with the bandwidth of $180° - 37° \leq |\Delta\Phi| \leq 180° - 37°$. Moreover, the minimum value of $|R_{yy}|$ almost appears at the frequency where $\Delta\Phi$ is equal to 180°, further proving the correctness of the proposed criterion. According to Eq. (5), when $\Delta\Phi$ is approximated to 180°, the reflected phase for R_{xy} will become $\Phi_{xy} = \Phi_u$. Therefore, PCR is determined by the phase difference of $\Delta\Phi$, while the reflected phase of the cross-polarized mode depends on Φ_u.

Given this, it is relatively important to determine the factors that primarily influence the phases of Φ_u and Φ_v. For this reason, Figs. 2(e) and 2(f) show the surface currents under the illumination of u and v polarized waves. It is clear that the connecting rod of the quasi-l-shaped metal pattern resonates when the v polarized wave impinges on the element, whereas the lateral arcs resonate when the element is impinged by the u polarized wave. In other words, Φ_v is influenced by the size of the connecting rod and Φ_u depends on that of the arcs. Therefore, we can choose the proper parameters of r and φ to introduce an abrupt phase change for the cross-polarized reflection mode, which is also denoted by Φ_{xy}. Further, if we set the element as depicted in Fig. 2(d), the reflection coefficients in the x-o-y coordinate system will become

$$R_{yx} = \frac{\exp(j\Phi_v) - \exp(j\Phi_u)}{2}. \tag{8}$$

Comparing Eq. (8) with Eq. (5), we conclude that the reflected phase difference will remain at 180° when the metallic pattern is rotated by $\theta = 45°$ and $\theta = -45°$. That is, through a mirror operation of the top metallic pattern with respect to the y axis while keeping other parameters unchanged, the reflection phase exhibits an additional phase jump of 180°. Therefore, if we want to obtain a full 360° phase coverage, we only need to obtain a phase span of 180° by modifying other geometric parameters of the two types of elements with $\theta = 45°$ and $\theta = -45°$. Following this method, we first adjust the opening angle φ of the arc to acquire an adequate phase change. Figs. 4(a) and 4(b) show the reflection amplitude and phase of R_{xy} by modifying φ. Clearly, high reflectivity is obtained from 10 to 22 GHz and the phase curves at different frequencies are almost parallel to each other, which will contribute to a broad operation bandwidth of the resulting focusing MS. Unfortunately, only a phase span of 140° is achieved when φ varies from 70° to 164°. To expand the phase coverage, we further tune the arc radius r by fixing $\varphi = 164°$. As expected in Figs. 4(c) and 4(d), a high reflection rate and an additional phase span of 40° are achieved when r varies from 1.6 to 1.9 mm. That is, a phase span of 180° is almost achieved by modulating the size parameters of r and φ as well as introducing a proper approximation. In addition, we can further conclude that a phase span of 360° for the cross-polarized reflection wave is obtained when r, θ, and φ are adjusted. Finally, the angular stabilities, including reflectivity stability and phase stability of the cross-polarized reflection wave for the proposed meta-atom, are shown in Figs. 4(e) and 4(f).

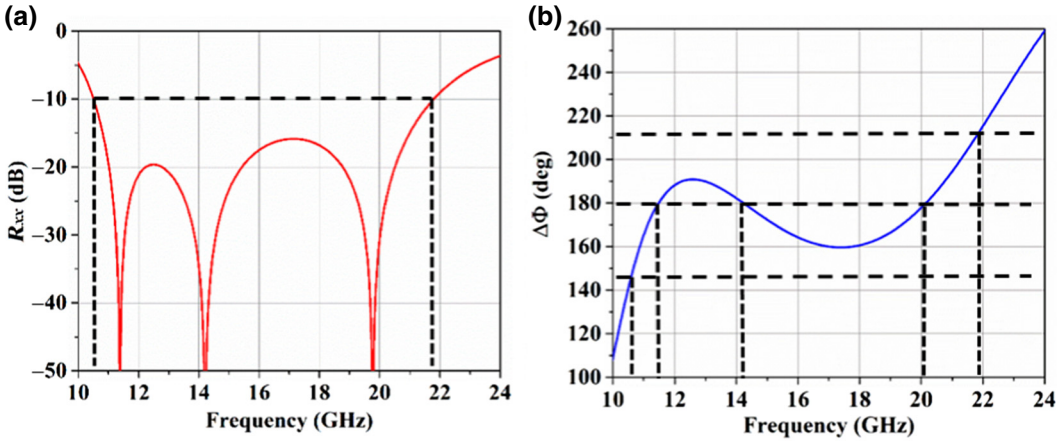

FIG. 3. Reflectivity and phase difference. (a) The copolarized reflectivity (Rxx) under the illumination of an x polarized wave. (b) The phase difference between Φ_u and Φ_v which are achieved by illuminating the element with u and v polarized wave. The numerical simulations are all carried out with unit-cell boundary along four walls in the x and y directions in CST Microwave Studio.

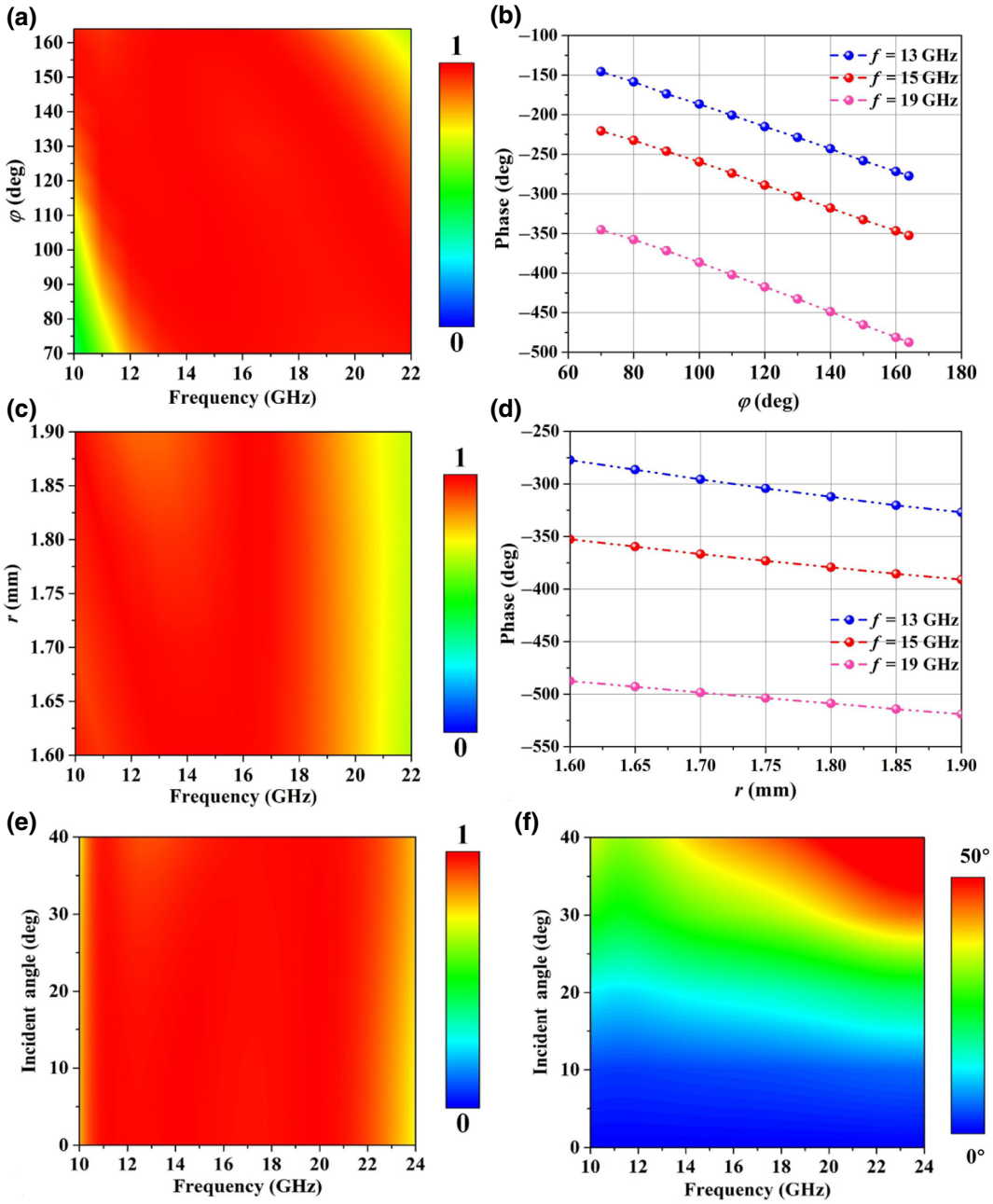

FIG. 4. (a) Amplitude and (b) phase of *Rxy* as a function of frequency and rotation angle φ with $r = 1.6$ mm and $\theta = 45°$. (c) Amplitude and (d) phase of *Rxy* as a function of frequency and the parameter r with $\varphi = 164°$ and $\theta = 45°$. (e) Amplitude and (f) fluctuating phase range of *Rxy* as a function of frequency and incident angle with $r = 1.6$ mm, $\varphi = 120°$, and $\theta = 45°$. Here, the meta-atom is excited by a y polarized wave in CST Microwave Studio with the unit-cell boundary condition.

As can be seen, the reflectivity of the cross-polarized mode can always hold a high level in the bandwidth of 10–22 GHz, even when the incident angle is up to 40°. Although the reflection phase of crosspolarization fluctuates more at higher frequencies, the fluctuation range is always below 50° across the bandwidth of 10–24 GHz, which correspondingly lays the foundation for the application of the focusing MS to a high gain antenna in the next session.

III. FOCUSING METASURFACE AND ITS CASSEGRAIN APPLICATION

A. Broadband focusing metasurface and its performance

Based on the unique features of the element, we can configurate a focusing MS lens with a simultaneous high-efficiency cross-PC ability. As shown in Fig. 5(a), a phase profile is generated by taking the preset focal length of

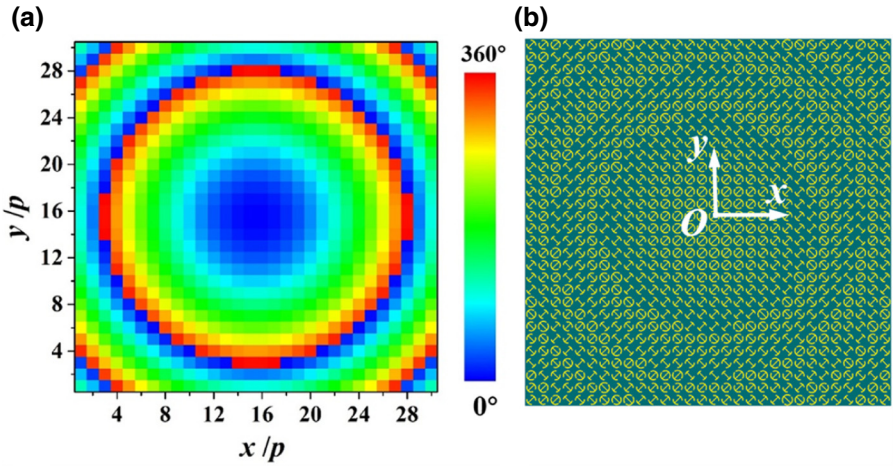

FIG. 5. (a) Phase profile of the devised focusing MS. (b) The configured polarization conversion focusing MS.

$F = 90$ mm and an $m \times n$ matrix given by the phase distribution $\Phi(m,n) = (2\pi/\lambda)(\sqrt{(mp)^2 + (np)^2 + F^2} - F)$. Note that p is the element size, while $\Phi(m,n)$ is the discrete form of the abovementioned phase profile of $\Phi(x,y) = (2\pi/\lambda)(\sqrt{x^2 + y^2 + F^2} - F)$. Corresponding the phase blocks to concrete elements, we configure a MS lens as shown in Fig. 5(b). With the matrix size set to 30×30, the MS lens occupies a size of 150×150 mm^2.

Then, we numerically simulate the performance of the MS lens in CST Microwave Studio® with incidence of the x polarized plane wave and open (add space) boundary conditions set in all directions. The power distribution on the x-o-z plane is unambiguously shown in Fig. 6(a), where a focal point with a certain focal length is depicted. To demonstrate the accurate location of the focal point, the normalized power distribution on the line ($x = 0$, $y = 0$) is calculated and depicted in Fig. 6(b). Apparently, the power peaks at $z = 79$ mm, which is not the location of

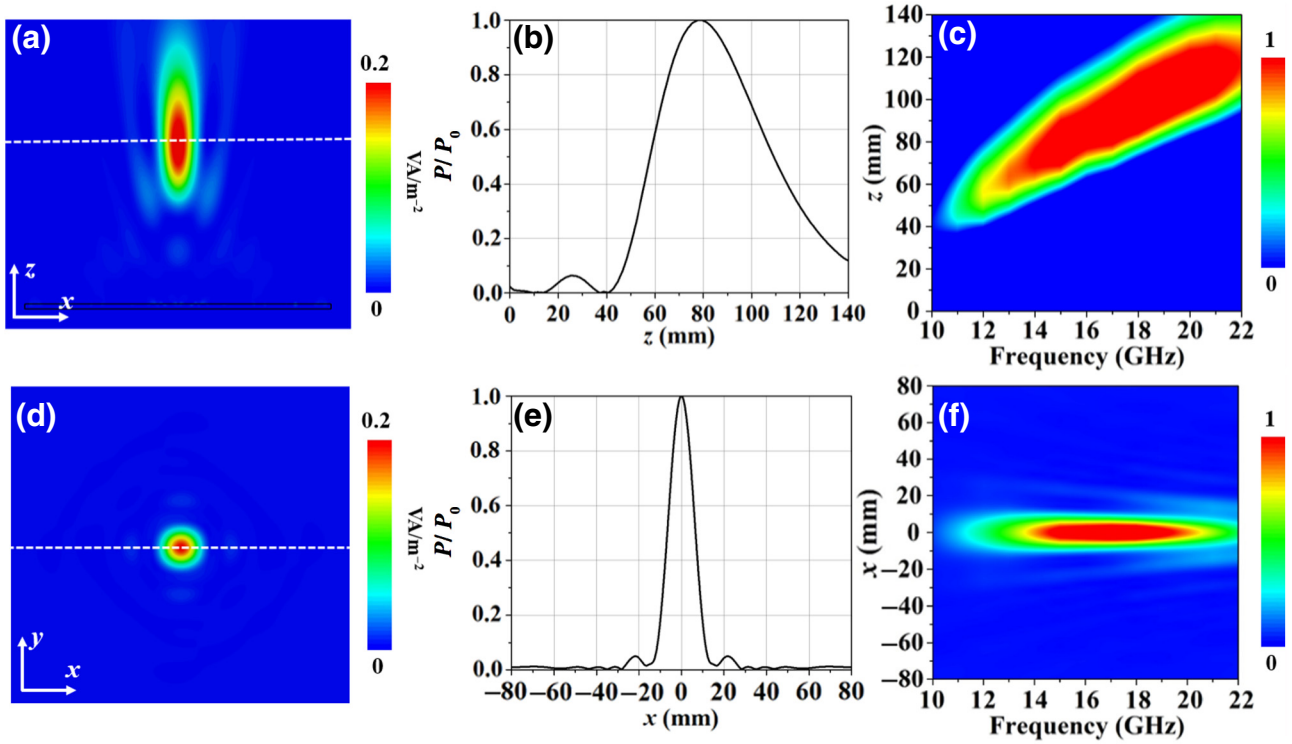

FIG. 6. Simulated performances of the focusing MS prototype. (a) Power distribution on the x-o-z plane at 15 GHz. (b) Normalized power distribution on the line ($x = 0$, $y = 0$) that corresponds to the dashed line in (a). (c) Normalized power distribution as a function of frequency and distance to the surface on the line ($x = 0$, $y = 0$). (d) Power distribution on the plane of $z = 90$ mm at 15 GHz. (e) Normalized power distribution on the line ($y = 0$, $z = 90$ mm) that corresponds to the dashed line in (d). (f) Normalized power distribution as a function of frequency and location on the line ($y = 0$, $z = 90$ mm).

the designed focal point. This is because our calculated peak power shows the location where the maximum E field is rather than the location where the "phase focal point" is. In Ref. [36], it has been firmly proven that the distance from the point where the power peaks to the surface is shorter than the so-called "phase focal length," which is set as $F = 90$ mm in our design. To show the operating bandwidth of the planar MS lens, the power distributions on the line ($x = 0$, $y = 0$) are calculated at different frequencies and then synthesized to form a two-dimensional (2D) map as shown in Fig. 6(c). Undoubtedly, a good focusing effect can be observed from 13 to 21 GHz and the focal length is increased when the frequency increases. The deviation of the focal point is a consequence of the dispersive phase profile of the focusing MS, which has been widely illustrated in much literature [37,38]. Figure 6(d) shows the calculated power distribution on the surface of $z = 90$ mm at 15 GHz. Apparently, the power

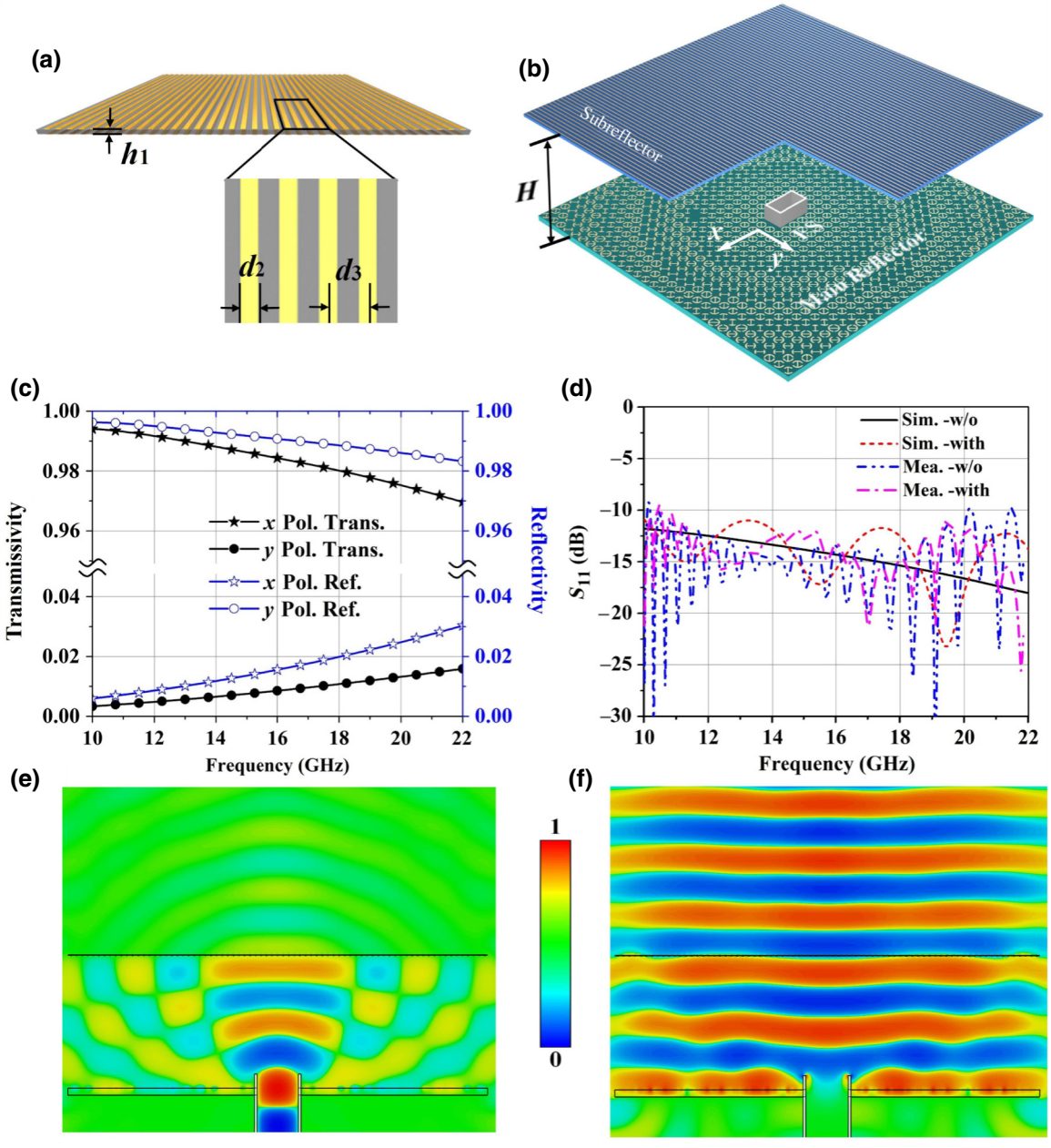

FIG. 7. (a) Designed polarized grating and its specific parameters. (b) The assembled Cassegrain antenna in which the waveguide feed has a broad wall of 15.2 mm and a narrow wall of 7.6 mm. Parts of the subreflector are removed to give a clear view. (c) Transmissivity and reflectivity of the polarized grating for x and y polarized incidence. (d) Simulated and measured reflection coefficient of the waveguide FS with and without (w/o) sub- and main reflectors. (e) E field distribution (E_y) on the x-o-z plane. (e) E field distribution (E_x) on the x-o-z plane.

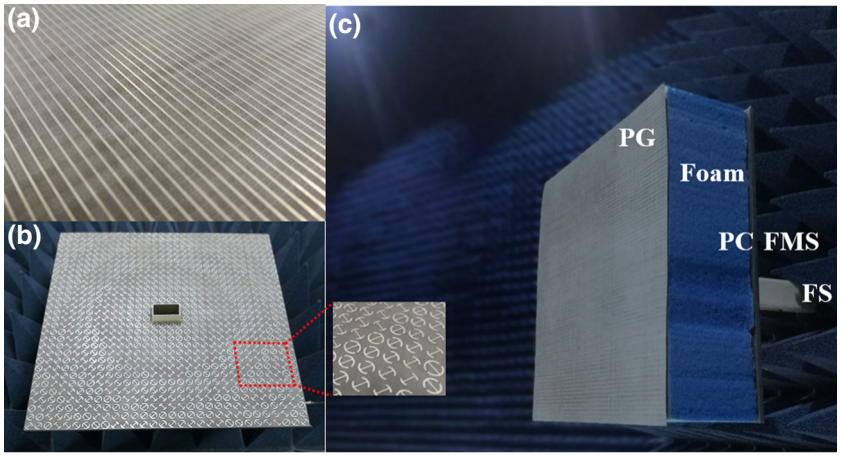

FIG. 8. Fabricated sample and measured setup. (a) The fabricated PG. (c) The polarization conversion focusing MS (PC FMS) with a waveguide FS embedded in the center area. (c) Assembled antenna and its measured setup.

on the surface converges to the center point, indicating a good focusing performance of the designed MS lens. To further evaluate the focusing effect, we calculate and then depict the normalized power distribution on the line ($y = 0$, $z = 90$ mm). The focal width, which is defined as the width over which the peak power drops by half, is equal to 11 mm (0.55λ at 15 GHz), which is close to the diffraction limit (approximately 0.5λ), correspondingly illustrating a good focusing effect. Finally, the power distributions on the line ($y = 0, z = 90$ mm) at different frequencies are synthesized into a 2D map as shown in Fig. 6(f). Clearly, powers are well focused in the central area from 13 to 21 GHz, which is conducive to forming a broad-band high-gain lens antenna [39,40] when a point source is fixed at the focal point (0, 0, 90 mm).

B. Cassegrain application of the focusing metasurface

According to the theory of light reversibility, focusing MSs can also convert spherical waves emitted from the focal point into plane waves when the constituent elements are not sensitive to the incident angle of an impinging

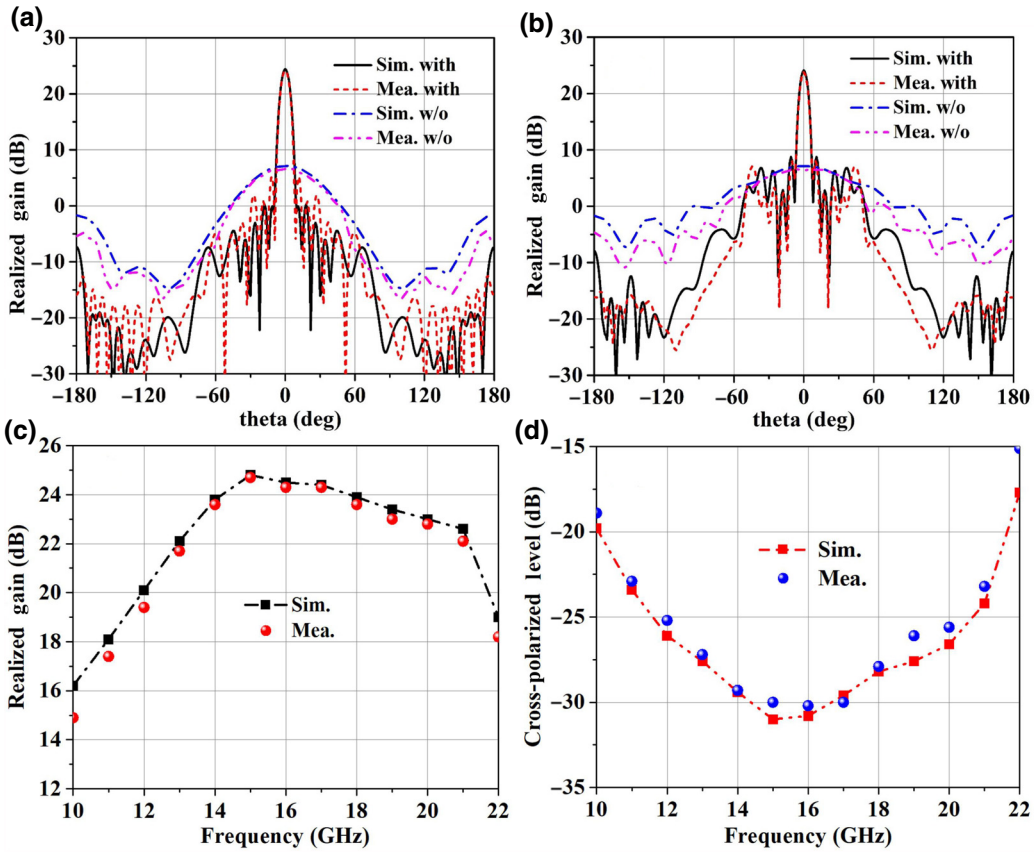

FIG. 9. Performances of the Cassegrain antenna. (a) Far-field patterns on the *x-o-z* plane with or without (w/o) the Cassegrain sample at 15 GHz. (b) Far-field patterns on the *y-o-z* plane with or without (w/o) the Cassegrain sample at 15 GHz. (c) Realized gain and (d) polarized isolation of the antenna versus frequency.

TABLE I. Performance compared with other reflectarrays.

Ref. No.	Form	Pol.	F/D	3-dB GBW	−20 dB IBW	Peak AE
This work	C-RA	linear	0.32	48%	68.4%	42.7%
[41]	C-RA	linear	0.2	narrow	narrow	33.3%
[32]	C-RA	linear	0.31	narrow	narrow	22.4%
[42]	RA	circular	0.97	47.8%	...	60%

RA represents reflectarray, C-RA represents Cassegrain reflectarray. F/D denotes the ratio of antenna profile to antenna diameter. In addition, GBW corresponds to gain bandwidth, while IBW shows polarization isolation bandwidth. AE represents aperture efficiency.

wave. As for our designed focusing MS, it can also convert linearly polarized incidence into its cross-polarized mode in addition to wave-front engineering. Based on the design method we introduced in Sec. II, a PG, as shown in Fig. 7(a), can be employed to form a planar Cassegrain antenna by combining it with the designed focusing MS, which is unambiguously depicted in Fig. 7(b). The metallic gratings, which are designed with a grating width of $d_2 = 0.4$ mm and a grating gap of $d_3 = 2$ mm, are etched on both the top and bottom of a substrate with a relative dielectric constant of 2.65, loss tangent of 0.003, and thickness of $h_1 = 0.2$ mm. To easily assemble with the focusing MS, the PG is designed with a size of 150×150 mm^2. In Fig. 7(c), we show the simulated transmissivity and reflectivity of the gratings for an orthogonally polarized wave. As expected, the x polarized wave always has high transmissivity, while the y polarized counterpart has high reflectivity in the frequency range of 10–22 GHz. The planar Cassegrain antenna, as shown in Fig. 7(b), is installed with the devised PG acting as the subreflector, the designed focusing MS as the main reflector, and an open waveguide as a point FS. The outstretched length of the FS is fixed to 5 mm. The distance between the sub- and main reflectors, which is the profile height of the planar Cassegrain antenna, is determined to be $H = 47.5$ mm according to Eq. (2). Figure 7(d) demonstrates the simulated and measured reflection coefficients of the FS with and without the designed surfaces, which unanimously show a well-matched impedance bandwidth of 10–22 GHz. Then, we show the E field distribution on the x-o-z plane to verify the physics behind it, as illustrated in Fig. 1(d). Unambiguously, the E field distribution of E_y in Fig. 7(e) and the counterpart of E_x in Fig. 7(f) validate the ability of both the PC and wave-front manipulation of incident waves.

In addition to numerical simulation, the MS samples, including the PG and PC FMS, are all fabricated with a standard print circuit board (PCB) technique and then measured in a microwave anechoic chamber to avoid unwanted interfering reflection from the surroundings. The fabricated polarized grating prototype shown in Fig. 8(a) is assembled with the focusing MS [shown in Fig. 8(b)] to form the planar Cassegrain antenna as shown in Fig. 8(c). In Figs. 9(a) and 9(b), we show the simulated and measured far-field patterns on the x-o-z and y-o-z planes [the described planes are all under the x-o-y coordinate system depicted in Fig. 7(b)]. Unanimously, the measured results demonstrate that the Cassegrain antenna has a directive radiation pattern with a peak gain of 24.8 dB, a 3-dB beam width of 7°, and a side lobe level of −13.4 dB. In addition, by virtue of adopting of a PG, the cross-polarized level is suppressed to −30.4 dB at 15 GHz. To show the operating bandwidth of the assembled Cassegrain antenna, the far-field performances at 10–22 GHz are depicted in Figs. 9(c) and 9(d) in terms of gain and cross-polarized levels, respectively. It is explicitly shown that the measured 3-dB gain variation bandwidth is from 13 to 21.2 GHz (48%). Furthermore, a −20 dB cross-polarization level bandwidth is utilized to evaluate the polarization purity characteristic of the antenna. Clearly, a 68.4% −20 dB cross-polarization level bandwidth is achieved from 10.4 to 21.2 GHz. Moreover, the profile of the Cassegrain antenna is correspondingly shrunk to 47.5 mm, which is only 0.53 times the focal length, which enables the antenna to be more compact and more applicable in many scenarios, such as satellite communication, radar systems, and so on.

To further validate the advantages of the proposed Cassegrain antenna, comparisons between the proposed design and other reported reflectarrays are given in Table I. Obviously, all these Cassegrain reflectarrays have a low ratio of antenna profile to antenna diameter (F/D) ratio, consequently leading to a lower antenna profile, which is actually by virtue of introducing the subreflector. However, the reflectarray, by contrast, has a broader operating bandwidth and higher peak aperture efficiency. Notably, the proposed Cassegrain antenna possesses not only a low profile, but also a broad gain and polarization isolation bandwidth. In addition, the proposed antenna has a higher aperture efficiency compared to the reported Cassegrain reflectarrays despite being slightly lower than the reflectarray in Ref. [42]. Nevertheless, the proposed antenna herein unambiguously achieves good overall radiation performances in terms of gain bandwidth and polarization purity, as well as aperture efficiency.

IV. CONCLUSIONS

In summary, a broad-band cross-PC meta-atom is proposed to realize a broad-band focusing MS with a simultaneous PC effect. This is then applied to form a Cassegrain antenna with high gain, high-polarization purity, and a low profile. The PC principle is first analyzed and then applied to optimize a broad-band PC meta-atom with simultaneous phase manipulation. Based on the optimized meta-atom, a PC MS lens is constructed and then applied to form a planar Cassegrain antenna by combining with a PG plate. Consistent numerical and experimental results both validate the good performances of the final assembled antenna, which are in terms of a 3-dB gain bandwidth of 48% (13–21.2 GHz) and a −20 dB cross-polarization level bandwidth of 68.4% (10.4–21.2 GHz). In addition, the profile is much shorter than the focal length, consequently enabling the antenna to be more practical in real word applications.

ACKNOWLEDGMENTS

National Natural Science Foundation of China (NSFC) under Grants No. 61671231 and No. 61871394; National Key Research and Development Program of China under Grant No. 2017YFA0700201; Aviation Science Foundation of China under Grant No. 20161996009; Key Program of National Natural Science Foundation of Shaanxi Province under Grant No. 2017KJXX-24, and China Postdoctoral Science Foundation under Grant No. 2017M620202.

Wen-Long Guo and Ya-Qiang Zhuang contributed equally.

[1] N. Yu, P. Genevet, M. A. Kats, F. Aieta, J.-P. Tetienne, F. Capasso, and Z. Gaburro, Light propagation with phase discontinuities: Generalized laws of reflection and refraction, Science **334**, 333 (2011).

[2] Z. C. Li, W. W. Liu, H. Cheng, J. Liu, S. Chen, and J. Tian, Simultaneous generation of high efficiency broadband asymmetric anomalous refraction and reflection waves with few-layer anisotropic metasurface, Sci. Rep. **6**, 35485 (2016).

[3] T. Cai, S. W. Tang, G. M. Wang, H. X. Xu, S. L. Sun, Q. He, and L. Zhou, High-performance bifunctional metasurfaces in transmission and reflection geometries, Adv. Opt. Mater. **5**, 1600506 (2017).

[4] T. Meissner and F. J. Wentz, Polarization rotation and the third stokes parameter: The effects of spacecraft attitude and Faraday rotation, IEEE Trans. Geosci. Remote Sens. **44**, 506 (2006).

[5] H. X. Xu, S. Ma, X. Ling, X.-K. Zhang, S. Tang, T. Cai, S. Sun, Q. He, and L. Zhou, Deterministic approach to achieve broadband polarization independent diffusive scatterings based on metasurfaces, ACS Photonics **5**, 7b01036 (2018).

[6] B. Sima, K. Chen, X. Luo, J. Zhao, and Y. Feng, Combining Frequency-Selective Scattering and Specular Reflection Through Phase-Dispersion Tailoring of a Metasurface, Phys. Rev. Appl. **10**, 064043 (2018).

[7] L. Zhang, S. Mei, K. Huang, and C.-W. Qiu, Advances in full control of electromagnetic waves with metasurfaces, Adv. Opt. Mater. **4**, 818 (2016).

[8] H. X. Xu, S. Tang, G. Wang, T. Cai, W. Huang, Q. He, S. Sun, and L. Zhou, Multifunctional microstrip array combining a linear polarizer and focusing metasurface, IEEE Trans. Antennas Propag. **64**, 3676 (2016).

[9] X. C. Zhu, W. Hong, K. Wu, H. J. Tang, Z. C. Hao, J. X. Chen, and G. Q. Yang, A novel reflective surface with polarization rotation characteristic, IEEE Antennas Wirel. Propag. Lett. **12**, 968 (2013).

[10] Y. Jia, Y. Liu, W. Zhang, and S. Gong, Ultra-wideband and high-efficiency polarization rotator based on metasurface, Appl. Phys. Lett. **109**, 051901 (2016).

[11] A. D. Rubio, V. S. Asadchy, A. Elsakka, and S. A. Tretyakov, From the generalized reflection law to the realization of perfect anomalous reflectors, Sci. Adv. **3**, e1602714 (2017).

[12] K. Chen, Y. Feng, F. Monticone, J. Zhao, B. Zhu, T. Jiang, L. Zhang, Y. Kim, X. Ding, S. Zhang, A. Alu, and C.-W. Qiu, A reconfigurable active huygens' metalens, Adv. Mater. **29**, 1606422 (2017).

[13] X. Li, S. Xiao, B. Cai, Q. He, T. J. Cui, and L. Zhou, Flat metasurfaces to focus electromagnetic waves in reflection geometry, Opt. Lett. **37**, 4940 (2012).

[14] H. X. Xu, H. W. Liu, X. Ling, Y. Sun, and F. Yuan, Broadband vortex beam generation using multimode Pancharatnam–Berry metasurface, IEEE Trans. Antennas Propag. **65**, 7378 (2017).

[15] G. Ding, K. Chen, T. Jiang, B. Sima, J. Zhao, and Y. Feng, Full control of conical beam carrying orbital angular momentum by reflective metasurface, Opt. Express **26**, 20990 (2018).

[16] M. Q. Mehmood, S. Mei, S. Hussain, K. Huang, S. Y. Siew, L. Zhang, T. Zhang, X. Ling, H. Liu, J. Teng, A. Danner, S. Zhang, and C.-W. Qiu, Visible-Frequency metasurface for structuring and spatially multiplexing optical vortices, Adv. Mater. **28**, 2533 (2016).

[17] D. Schurig, J. J. Mock, B. J. Justice, S. A. Cummer, J. B. Pendry, A. F. Starr, and D. R. Smith, Metamaterial electromagnetic cloak at microwave frequencies, Science **314**, 977 (2006).

[18] H. X. Xu, L. Zhang, Y. J. Kim, G. M. Wang, X. K. Zhang, Y. M. Sun, X. H. Ling, H. W. Liu, Z. N. Chen, and C. W. Qiu, Wavenumber-splitting metasurfaces achieve multichannel diffusive invisibility, Adv. Opt. Mater. **6**, 1800010 (2018).

[19] G. Moreno, A. B. Yakovlev, H. M. Bernety, D. H. Werner, H. Xin, A. Monti, F. Bilotti, and A. Alù, Wideband elliptical metasurface cloaks in printed antenna technology, IEEE Trans. Antenn. Propag. **66**, 3512 (2018).

[20] J. Xu, R. Li, J. Qin, S. Wang, and T. Han, Ultra-broadband wide-angle linear polarization converter based on H-shaped metasurface, Opt. Express **26**, 20913 (2018).

[21] B. Q. Lin, J.-X. Guo, P. Chu, W.-J. Huo, Z. Xing, B.-G. Huang, and L. Wu, Multiple-Band Linear-Polarization

Conversion and Circular Polarization in Reflection Mode Using a Symmetric Anisotropic Metasurface, Phys. Rev. Appl. **9**, 024038 (2018).

[22] H. F. Ma, G. Z. Wang, G. S. Kong, and T. J. Cui, Broadband circular and linear polarization conversions realized by thin birefringent reflective metasurfaces, Opt. Mater. Express **4**, 1717 (2014).

[23] X. Ding, F. Monticone, K. Zhang, L. Zhang, D. Gao, S. N. Burokur, A. de Lustrac, Q. Wu, C. W. Qiu, and A. Alù, Ultrathin Pancharatnam-Berry metasurface with maximal cross-polarization efficiency, Adv. Mater. **27**, 1195 (2015).

[24] H. Y. Shi, A. X. Zhang, S. Zheng, J. X. Li, and Y. S. Jiang, Dual-band polarization angle independent 90° polarization rotator using twisted electric-field-coupled resonators, Appl. Phys. Lett. **104**, 034102 (2014).

[25] X. Gao, X. Han, W. P. Cao, H. O. Li, H. F. Ma, and T. J. Cui, Ultra-wideband and high-efficiency linear polarization converter based on double V-shaped metasurfaces, IEEE Trans. Antenn. Propag. **63**, 3522 (2015).

[26] J. C. Zhao and Y. Z. Cheng, Ultra-broadband and high-efficiency reflective linear polarization convertor based on planar anisotropic metamaterial in microwave region, Optik (Stuttg.) **136**, 52 (2017).

[27] Y. Huang, L. Yang, J. Li, Y. Wang, and G. Wen, Polarization conversion of metasurface for the application of wide band low-profile circular polarization slot antenna, Appl. Phys. Lett. **109**, 054101 (2016).

[28] H. L. Zhu, S. W. Cheung, X. H. Liu, and T. I. Yuk, Design of polarization reconfigurable antenna using metasurface, IEEE Trans. Antenn. Propag. **62**, 2891 (2014).

[29] Y. Zheng, Y. Zhou, J. Gao, X. Cao, H. Yang, S. Li, L. Xu, J. Lan, and L. Jidi, Ultra-wideband polarization conversion metasurface and its application cases for antenna radiation enhancement and scattering suppression, Sci. Rep. **7**, 16137 (2017).

[30] H. P. Li, G. M. Wang, T. Cai, J. G. Liang, and X. J. Gao, Phase- and amplitude-control metasurfaces for antenna main-lobe and sidelobe manipulations, IEEE Trans. Antenn. Propag. **66**, 5121 (2018).

[31] H.-X. Xu, G. Hu, L. Han, M. Jiang, Y. Huang, Y. Li, X. Yang, X. Ling, L. Chen, J. Zhao, and C.-W. Qiu, Chirality-assisted high-efficiency metasurfaces with independent control of phase, amplitude and polarization, Adv. Opt. Mater. **7**, 1801479 (2019).

[32] J. Zhao, H. Li, X. Yang, W. Mao, B. Hu, T. Li, H. Wang, Y. Zhou, and Q. Liu, A compact Ka-band monopulse cassegrain antenna based on reflectarray elements, IEEE Antennas Wireless Propag. Lett. **17**, 193 (2018).

[33] X. Liu, J. Deng, K. F. Li, Y. Tang, M. Jin, J. Zhou, X. Cheng, W. Liu, and G. Li, Planar Cassegrain-type schwarzschild objective with optical metasurfaces, arXiv: 1807.01143 (2018).

[34] T. Cai, G.-M. Wang, H.-X. Xu, S.-W. Tang, H. Li, J.-G. Liang, and Y.-Q. Zhuang, Bifunctional Pancharatnam-Berry metasurface with high-efficiency helicity-dependent transmissions and reflections, Ann. Phys. **530**, 1700321 (2017).

[35] S. L. Jia, X. Wan, P. Su, Y. J. Zhao, and T. J. Cui, Broadband metasurface for independent control of reflected amplitude and phase, AIP Adv. **6**, 045024 (2016).

[36] C. Saeidi and D. v. d. Weide, A figure of merit for focusing metasurfaces, Appl. Phys. Lett. **106**, 113110 (2016).

[37] A. Pors, M. G. Nielsen, R. L. Eriksen, and S. I. Bozhevolnyi, Broadband focusing flat mirrors based on plasmonic gradient metasurfaces, Nano Lett. **13**, 829 (2013).

[38] S. Wang, P. C. Wu, V.-C. Su, Y.-C. Lai, C. H. Chu, J.-W. Chen, S.-H. Lu, J. Chen, B. Xu, C.-H. Kuan, T. Li, S. Zhu, and D. P. Tsai, Broadband achromatic optical metasurface devices, Nat. Commun. **8**, 187 (2017).

[39] C. Mateo-Segura, A. Dyke, H. Dyke, S. Haq, and Y. Hao, Flat Luneburg lens via transformation optics for directive antenna applications, IEEE Trans. Antenn. Propag. **62**, 1945 (2014).

[40] Q. Wu, Z. H. Jiang, O. Quevedo-Teruel, J. P. Turpin, W. Tang, and Y. Hao, Transformation optics inspired multibeam lens antennas for broadband directive radiation, IEEE Trans. Antenn. Propag. **61**, 5910 (2013).

[41] G. B. Wu, S. W. Qu, S. Yang, and C. Ma, *European Conference on Antennas & Propagation IEEE* (2017), p. 978

[42] L. Zhang, S. Gao, Q. Luo, and W. T. Li, Single-Layer wideband circularly polarized high-efficiency reflectarray for satellite communications, IEEE Trans. Antennas Propag. **65**, 4529 (2017).